Deriving hard carbon material from biowaste for Sodium Ion Battery and enhancing the electrochemical performance via nitrogen doping.

Maksat Maratov, B.Eng

Submitted in fulfilment of the requirements

for the degree of Master of Science in

Chemical & Materials Engineering

NAZARBAYEV UNIVERSITY

School of Engineering and Digital Science

Department of Chemical & Materials Engineering

Nazarbayev University

53 Kabanbay Batyr Avenue,

Astana, Kazakhstan, 010000

Supervisors: Professor Aishuak Konarov

April 2020-2023

DECLARATION

I hereby, declare that this manuscript, entitled “Deriving hard carbon material from biowaste for Sodium Ion Battery and enhancing the electrochemical performance via nitrogen doping”, is the result of my own work except for quotations and citations which have been duly acknowledged. I also declare that, to the best of my knowledge and belief, it has not been previously or concurrently submitted, in whole or in part, for any other degree or diploma at Nazarbayev University or any other national or international institution.

Name: Maksat Maratov
Date: 07.04.2023

Abstract

The current positive trend in the growth of electricity consumption is increasingly pushing humanity to develop and improve the method of obtaining energy from renewable energy sources. One of the system energy optimizations is Grid storage technology. But unfortunately, due to the high price of lithium-ion batteries, these technologies are difficult to pay off. Sodium-ion batteries are considered one of the most promising and cheapest alternatives to replace lithium-ion batteries in Grid storage technology. The limiting factor in the development of sodium-ion batteries is the anode, due to the large ionic radius, sodium ions cannot intercalate into graphite. Hard carbon is the favorite for sodium-ion batteries. Until today, the exact mechanism of the reaction of hard carbon and sodium has not yet been deduced. Studying hard carbon, it was found that doping with heteroatoms can improve the structure for the free penetration of sodium ions into the internal structure of the material. In this work, hard carbon was synthesized from biowaste cherries. The effect of doping hard carbon with nitrogen atoms was studied using urea as a precursor. The result showed that carbon doping improved the hard carbon capacity from 206 mAh g^{-1} to 274 mAh g^{-1} at 20 mA g^{-1}. Moreover, hard carbon doped with nitrogen showed a superior capacitance of 110 mAh g^{-1} at a 1 A current rate.

Acknowledgments

I would like to take this opportunity to express my gratitude to all those who have supported me. First of all, I want to thank my Professor and mentor prof. Konarov for allowing me to develop and helping me in all stages of my thesis. It was a great pleasure to work with him in the group. I also wanted to express my gratitude to my colleagues from the Advanced Energy Storage System and Functional Nanomaterials laboratory for the friendly team and cohesion in the team.

I want to express special thanks to the members of the Department of Chemical Engineering. Over the years, this place has become like home to me.

And the most important thing I want to say here is that I am grateful to my parents sister and Murka for their limitless support.

Table of content

List of Abbreviations

A	Amper, unit of measurement of electric current in the International System of Units.
AB	Acetylene black.
DFT	Density Function Theory.
GITT	Galvanostatic Intermittent Titration Technique.
ICE	Initial Columbic Efficiency.
kg	Kilogram, unit of weight.
LIB	Lithium Ion Battery.
mg	Milligram, unit of weight.
mAh	Mili Amper Hour, electrical capacity of the battery.
NMP	n-methyl-2-pyrrolidone.
PVDF	Polyvinylidene Fluoride.
SIB	Sodium Ion Battery.
SEM	Scanning Electron Microscopy.
TEM	Transmission Electron Microscopy.
V	Voltage.

List of Figures

List of Tables

Chapter 1 - Introduction

1.1. Challenges in electrical energy generation.

Nowadays electrical energy became essential to human existence. Contemporary human beings are electrical energy in every part of their life, from cooking to charging electric vehicles for transportation. To supply the required amount of energy for an intensive growth population without significant issues in the future is a huge challenge. According to the worldwide population, in the last 30 years, it increased from 5 billion to 8 billion [1]. The growth of the population indicates increasing energy demand. Currently, electrical energy consumption on average increases by 2.3% per year, and electricity consumption has doubled over the past two decades [2]. The major source of electrical energy coming from burning coal, oil and natural gas, and processing the primary source of energy could lead to the environmental problem[2]. The reduction of exhaust gases is one of the main challenges of 21 century, which is well stated in the Paris agreement in 2015 [3]. One way of reducing the burning of primary energy sources is developing a method of energy storage. Currently, the working method of storing energy is using rechargeable batteries.

1.2. The working principles of rechargeable battery.

The system of traditional rechargeable batteries consists of a positive electrode - anode, a negative electrode - cathode, a separator and an electrolyte, graphical illustration represented in Figure 1. During the discharging of the cell, the degradation reaction between the active material and electrode occurs and the active material is converted to ions[4]. The mass transfer of released ions creates the flux of electrons in the outer circuit from the anode side to the cathode electrode. in the cathode the electrochemical reaction takes place and released ions intercalate into the electrode structure or create an alloy, the process continues until the potential of the two electrodes reaches the same value. The battery cell is filled with an ionic liquid to allow the mass transfer of ions. The separator acts as an electric insulation layer and it is used to prevent direct electron transfer through the system [5]. Nowadays, the most advanced commercialized energy-storing device is a lithium-ion battery (LIB). LIB is the most studied energy storing system, which was commercialized by Sony corporation in 1991 [6], [7]. Due to the high energy densities in comparison with nickel hydrate and lead-acid batteries, it is the optimal choice for electrical vehicle applications and portable electronic devices [8].

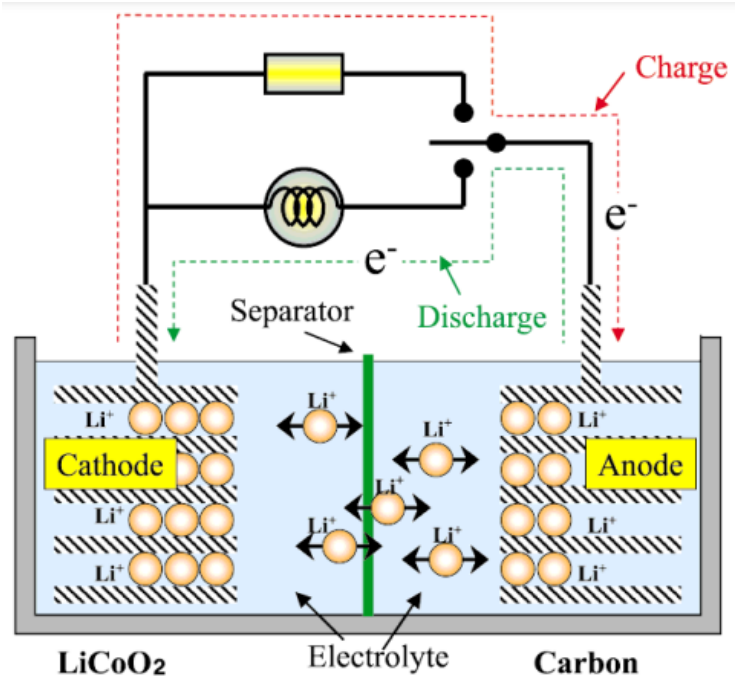

Figure 1. Schematic illustration of rechargeable battery. During charge ions migrate toward the anode, and during discharge the material ionized and migrates toward to cathode [4].

1.3. Lithium salts production and cost.

The development of the lithium ion-based energy storage device is strongly related to the source of the raw material. Lithium salt production has increased up to 10 times over the past 50 years, and lithium salt demand is expected to rise in the future with production growth 237 000 tons per year [9]. The cost of battery-grade lithium carbonate production cost increased 4 times from 2007 to 2017. The high cost of lithium-ion battery components is one of the factors that limiting in a big-scale application. The other factor is an uneven distribution of lithium resources on the earth's crust. 60% of lithium sources are located in Chile, 15.8% in China, 11.7% in the USA and 5.3% in Australia [10], [11]. An example of an uneven distribution problem is a crisis in China in 2016, the rapid development of the electric vehicle industry caused a high demand for lithium salts and the cost of carbonates reaches 22900 USD per ton [11]. The process of extracting lithium salt from the spodumene ore is a tedious process that requires several steps of alkaline and acid treatment [12]. Due to the mentioned limitations, it is urgently necessary to look for low-cost, secure, and long-cycle rechargeable batteries based on abundant resources.

1.4. Sodium ion battery as alternative for energy storage.

Sodium and lithium belong to one element family the energy-storing mechanism is similar. The development of the SIB energy storing system is in an early stage and requires further

investigation, and tremendous effort done toward the LIB system creates a solid foundation. The SIB is considered as one of the promising technologies for large-scale energy-storing applications which integrated with renewable energy sources, due to the high abundance of precursor materials. Also, the cost of the SIB battery is lower, since in LIB the copper foil is used as a current collector on the anode site due to the formation of the alloy between the aluminum collector and lithium, the advantage of sodium is it did not form an alloy with the aluminum collector[13]. The precursor materials for SIB are based on sodium salt which could be extracted from seawater, soda ash and trona [14]. The energy density of SIB is high and the redox potential of sodium is only 0.3V less than lithium. The main difference that creates challenges in SIB is the different volumes of the ions. The sodium ion is larger than lithium by 39%, which creates difficulties in storing active material in the electrode[15]. The larger ionic radius requires sufficient channels and spacing for free ion migration. Currently, the main purpose toward the development of highly safe SIB is the synthesis of suitable material for anode electrode.

Table 1.Comparison between sodium and lithium elements [16], [17].

	Sodium	Lithium
Abundance	23.6×10^3 mg kg^{-1}	20 mg kg^{-1}
Shannon ionic radius	1.02 A	0.76 A
Atomic weight	23 g mol^{-1}	6.9 g mol^{-1}
Redox potential	−2.7 V Na/Na^+	-3.04 V Li/Li^+
Melting temperature	97.7 ^oC	180.5 ^oC

1.5. The objectives of thesis work.

Developing promising anode material for sodium ion battery application with competitive electrochemical performance. The cherry pit is selected as the target material, no studies were done before on cherry pit for SIB application. Nitrogen doping was chosen as a method for tailoring defects and improving the electrochemical performance. Urea was selected nitrogen precursor, due to its high availability and low cost.

- Synthesis of anode materials from the cherry pit in different temperature ranges.
- Modifying the hard carbon structure by substitution of carbon with nitrogen.
- Performing characteristic analysis of synthesized materials, by using various analytical methods to observe the surface morphology, crystallinity structure and identifying electrochemical performance.

Chapter 2 - Literature review

2.1. Sodium ion battery anode.

There are several types of anodes, they are differentiated based on the electrochemical reaction between anode material and sodium ion. Based on the material, the sodium ion could intercalate to the layered structure, create an alloy or undergo electrochemical conversion.

In conversion type anode the crystalline structure of the anode is changing and phase transition takes place during releasing or uptake of the sodium ion. Generally, the conversion anode consists of transition metal and some anionic species, during charging of the battery sodium creates a chemical bond with anionic species and reduces the transition metal to the metallic state [16]. For example, in FeS_2, sodium reacts with sulfur and creates Na_2S and metallic iron produces. The general transition metals that are used in conversion anodes are oxides, sulfides, phosphides, and nitrides. The conversion type electrode provides high capacity, however, during the conversion, the voltage of the cell changes and creates voltage hysteresis which is a result of the overpotential required for the reaction between sodium and electrode [17]. As a result of voltage hysteresis, the columbic efficiency of the conversion-type electrode is low. Another important problem is the high volume expansion of the electrode, which cause electrode decomposition. As an example, Fe_3O_4 has a high first sodiation capacity of 720 mAh g^{-1} however during discharging a cell only 55% is a reversible capacity and low capacity retention is 75% after 50 cycles.

Alloying electrodes are prepared from materials that are able to form a reversible alloy with sodium, for example, tin, bismuth, lead, phosphorus, and antimony. During the formation alloy multiple electron exchange process takes place and sodium inserts into the crystalline and a new crystal structure is forming. The alloying electrodes have a high capacity, however, during the formation new crystal structure the volume expansion is huge. Also, they provide low energy density redox potential of the alloying electrode. For example redox potential of $Na_{15}Sn_4$ is 0.21V vs Na/Na^+, it has a high electrode capacity of 847 mAh g^{-1} and a volume expansion of 420% of the initial volume. The high volume expansion leads to the formation of a surface that is exposed to the electrolyte and during the charge/discharge process the continuous electrolyte degradation takes place [18].

Intercalation anode has a layered structure with sufficient interlayer distance for the insertion of the ions. The materials used for intercalation anode are layered transition metal oxides and carbonaceous material. Among the transition metal oxides, there are only a few structures that are suitable for sodium intercalation, because many of them have high intercalation potential which

exceeds the working band gap and could proceed the reaction of the electrolyte reduction. The sodium titanate has the lowest intercalation potential 0.3V vs Na/Na+, and the capacity of the electrode is 177 mAh g^{-1} at a current rate of 0.1A [19]. The electrochemical performance of porous TiO_2 reaches 248 mAh g^{-1} with 57% ICE [20]. For MXenes Ti_2CT_x, galvanostatic charge/discharge experiments provided a capacity of 175 $mAhg^{-1}$ with ICE 65% at a current rate of 20mAg^{-1} [21]. A carbonaceous anode is a material based on carbon, they are graphite, soft carbon and hard carbon, structure of carbonaceous material represented in Figure 2. Graphite is a material in a commercial application for LIB with 3.34A interlayer spacing between the graphene layers. For SIB application graphite is not appropriate, since the lack of binary intercalation compounds and the higher volume of the sodium ion, the sodium is unable to intercalate into the graphite structure [22]–[24]. From the theoretical approximation there concluded that 3.7A spacing is required for free sodium intercalation [25]–[27].

Figure 2. Schematic illustration of structure of a) graphite, b) soft carbon, c) hard carbon [29].

2.2. Storage mechanism for sodium ions into hard carbon.

The hard carbon is carbon allotropes that save the structure even in high temperatures 2500ºC, thus it classifies as non-graphitizable carbon. The inability of graphitization is a result of the presence of strong carbon-oxygen covalent bonds. Based on the complexity of the hard carbon structure several mechanisms sodiation mechanisms exists (Figure 3). The structure of hard carbon first proposed by Stevens and Dahn, described as a structure like "house of the card", this model characterizes the structure as randomly allocated and stacked aromatic fragments[28] [29]. Corresponding to this model the "insertion – adsorption" mechanism was proposed, where the sloping region described as insertion of alkali metals into stacked carbon layers and low energy plateau region described as adsorption of ions into nanopores. Later in 2011 Komaba et. al. confirmed "insertion – adsorption" mechanism, by analyzing sodiation and desodiation process of hard carbon by ex situ XRD. Increment of interplanar spacing during sodiation at 0.2V was proceed and this process was described as insertion of sodium into parallel graphene layer [30]. However, "insertion-adsorption" model had limitations, for example,

increment of temperature decreases the pore volume while the capacity of material increases. In 2012 the model “adsorption – intercalation” mechanism was proposed by Cao et al. There was proposed that high voltage region corresponds to adsorption of the sodium ion on surface of hard carbon and defective sites, while the low voltage plateau region corresponds to intercalation of sodium ions into graphitic layers [25]. Bommier et al. in 2015 supported theory of “asorption – intercalation” based on the result of sodium ion diffusivity coefficient obtained by GITT [31]. In the result was observed that in high voltage slope region the diffusivity coefficient is high, then there assumed that slope region corresponds to adsorption of sodium to easy assessable sites of hard carbon. In plateau region there was observed strong decrement of diffusivity coefficient, then assumed that plateau region corresponds to intercalation mechanism of sodium ions into hard carbon. Also, there was observed increment of diffusivity coefficient of sodium at voltage close to 0 V. This increment was described as sodium metal plating into nanopores, since the sodium plating does not affect on the graphene sheets spacing.

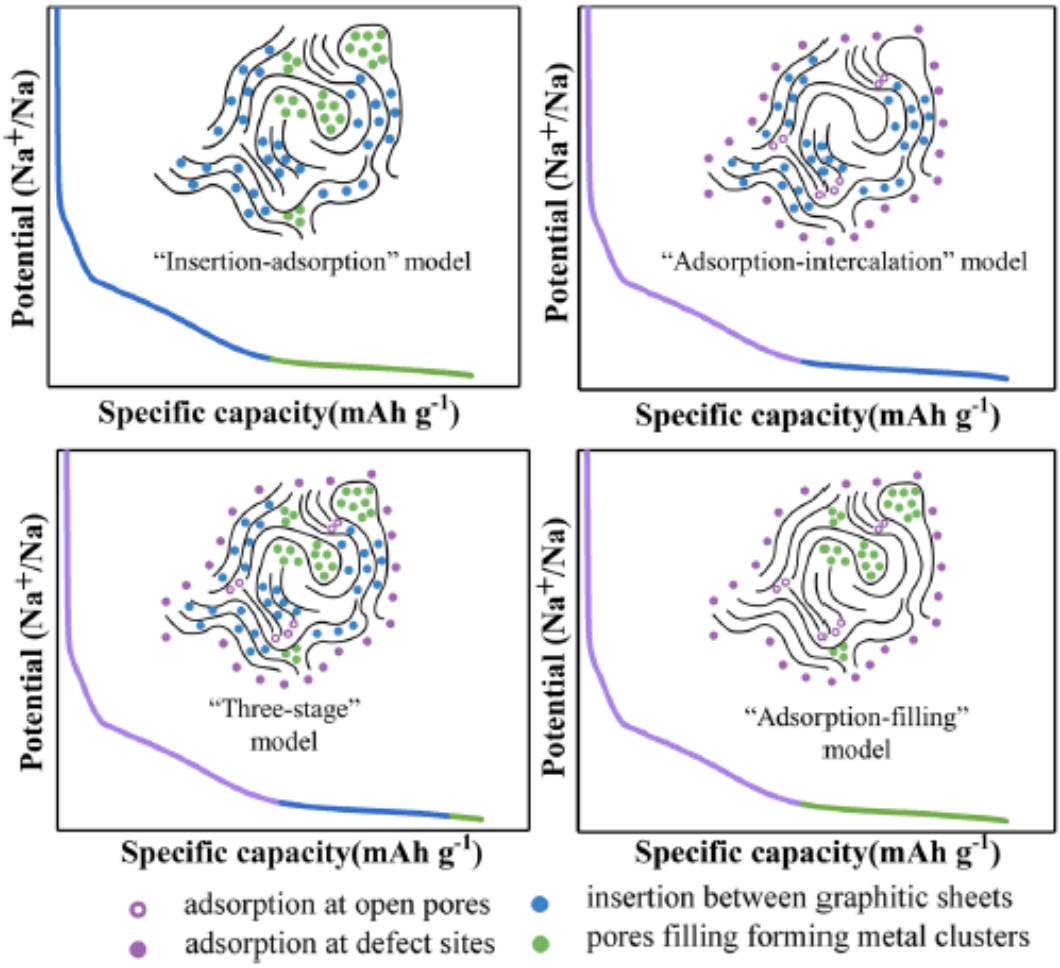

Figure 3. Sodium ions insertion mechanisms [32]**.**

2.3. Biomass derived hard carbon anode.

Recycling biomass is one step toward sustainable energy, and obtaining the right precursor that provides a good porous hierarchal structure is a current aim in hard carbon synthesis. Li Y. et al. studied waste cork as a precursor[33]. The material was carbonized at 800 ^{o}C 2h under the argon atmosphere, then it was washed with a solution of 30% hydrochloric acid and carbonized at a temperature range of 1200 ^{o}C – 2000 ^{o}C. In this study sample carbonized at 1600 ^{o}C show the best result of 360 mAh g^{-1} reversible capacity with 81% ICE at the current rate of 30 mA g^{-1}. Also here identified that higher temperature improves the inner and outer texture of the material, the effect of closed and open pores on the electrochemical performance. The effect of open nanopores observed on the ICE, and closed nanopores increase plateau capacity.

Zang N. et al. investigate the electrochemical performance of hard carbon derived by lotus stem [34]. The material was dried at 100 ^{o}C for 24 h and pyrolyzed in the argon atmosphere at 1200 ^{o}C, 1400 ^{o}C, 1600 ^{o}C. After heat treatment, it was washed with hydrofluoric acid solution and dried for 12 h. From the initial structure of the lotus stem the parallel channel arrays existed after heat treatment at 1600 ^{o}C, there explained that the existence of such structure positively affects on sodium insertion into the anode structure. There observed that with temperature increments the diameter of the hollowed parallel tube is decreased, due to the removal of heteroatoms such as oxygen. The hard carbon obtained at 1400 ^{o}C shows the best result with 351 mAh g^{-1} at 40 mA g^{-1} current density with 70% ICE.

Gaddam R. et al. studied cellulose nanofibers derived from the Australian native arid grass Triodia pungens [35]. The main purpose of this study was to optimize the synthesis temperature. The material was harvested and soaked in sodium hydroxide 2% (w/v) solution at 80 ^{o}C in order to reduce lignin content in the structure. After the delignification process, the sample was washed twice with a solution of sodium chloride and acetic acid for 1h, then the sample was placed into a high-pressure homogenizer at 700 bar. There observed that after delignification the content of lignin in the sample decreased from 20% to 2.5%, and cellulose content increased from 29% to 48%. The prepared sample undergoes thermal stabilization in the nitrogen atmosphere for 2 h at 240 ^{o}C with 5 ^{o}C min^{-1}, then the sample is heated up to 1000 ^{o}C with 5 ^{o}C min^{-1} for 2h. The obtained materials provide 366 mAh g^{-1} reversible capacity with 50% ICE at 20 mA g^{-1} current rate.

Han J. et.al. (2021) made a study on the energy storage mechanism of hard carbon [35]. The objective of this work was an analysis of the electrochemical behavior of the material at different scan rates. The Ni_3C (nickel carbide) was used. Material preparation started by dealloying nickel from

$Ni_{30}Mn_{70}$ cold roll sheet in the aqueous solution of 1M $(NH_4)_2SO_4$. Then obtained nanoporous nickel mixed with triethylene glycol in the aqueous solution of 25M NaOH at 230 ^oC for 14 hours. Synthesized nickel carbide then undergoes to dealloying reaction with iron chloride $FeCl_3$, as a result, porous carbon material was synthesized. The carbon material is heated at 900 ^oC, 1300 ^oC, and 1800 ^oC in an argon atmosphere. The electrochemical performance of materials was analyzed by cyclic voltammetry. Based on the response of current on different voltage change rates, the limiting region of mass transfer was identified. Based on the result in the high voltage change rate, the low current response indicates mass transfer limitation, while in the low voltage change rate, no sufficient changes occur on the current response. There identified three different regions based on the different mechanisms of sodium storage in hard carbon. There identified that the intercalation mechanism occurs in low voltage regions (<0.1 V), adsorption of the sodium in the defective site of the hard carbon proceeds in the medium voltage range (0.1-1.8 V), and surface adsorption.

Jin Y. et.al. (2018) proposed a theory on three storage mechanisms of hard carbon [36]. The main objective of their work was performing the galvanostatic intermittent titration technique (GITT) to identify the diffusion coefficient of the sodium ion and correlate it with the charge and discharge performance of the hard carbon. A precursor for hard carbon was used resorcinol formaldehyde, and it was carbonized at temperature range of 800 ^oC – 1600 ^oC. Based on GITT analysis Three different diffusion coefficient was obtained for a single material. Corresponding galvanostatic charge-discharge test, there identified their voltage ranges. The adsorption capacity region is 1-0.1 V, intercalation capacity is 0.1-0.03 V and pore filling capacity is 0.03-0 V. The adsorption capacity of the material decreases with temperature, it was argued on decreasing of the amount of active sites, edges and functional groups. There decided that adsorption capacity is related to the material surface. Intercalation capacity is increased with temperature and reached a maximum at 1300^oC and then decreased. The decrement of ICE is attributed to the shrinkage of the crystallite volume. Pore filling capacity increased with temperature and reached the maximum at 1300 ^oC and further increment of temperature was negatively affected. This phenomenon was also related to the volume decrement of graphitelike microcrystalytes, as a result, the diffusion of sodium ions was reduced.

Agrawal A. et al. studied the doping effect of hard carbon via first principle electronic structure calculation and molecular dynamics [36]. The DFT calculation was used to identify the volume expansion of the structure and MD was used to create the hard carbon structure by “liquid quenching”. During MD the hard carbon structure was simulated by creating a box with randomly allocated carbon and heating up to 8000 ^{o} K, then the system cooled with a high cooling rate of $4*10^{15}$ K s^{-1}. The

obtained structure was used in further DFT. The structure was modified by randomly substitution of the carbon with nitrogen 9%, for obtaining the sodiated structure, it was filled with sodium spheres and energy minimization was proceeded to obtain the optimal relaxed sodiated structure of nitrogen-doped hard carbon. The average performance of hard carbon was selected from different studies as 250 mAh g^{-1} and by simplification there assumed that the corresponding structure is NaC_9, and DFT calculation for volume expansion shows that 9% nitrogen substitution reduces the expansion from 21% to 7%. The interesting result that the author obtained is similar behavior of volume expansion on undoped hard carbon during lithiation and sodiation of nitrogen-doped hard carbon at an early stage of sodiation. In experimental work there prepared nano-spherical nitrogen-doped hard carbon by mixing sucrose with the sodium salt of poly (styrene sulphonic acid) and ammonium sulphate. The electrochemical performance shows that nitrogen substitution enhanced the capacity by 39% in comparison with bare nano-carbon spheres, and it provided a reversible capacity of 286 mAh g^{-1} with a capacity retention of 85%.

Chapter 3 - Methodology

In this chapter, the detailed procedure of material processing and analysis is reported. The visual representation of electrode preparation illustrated in Figure 4.

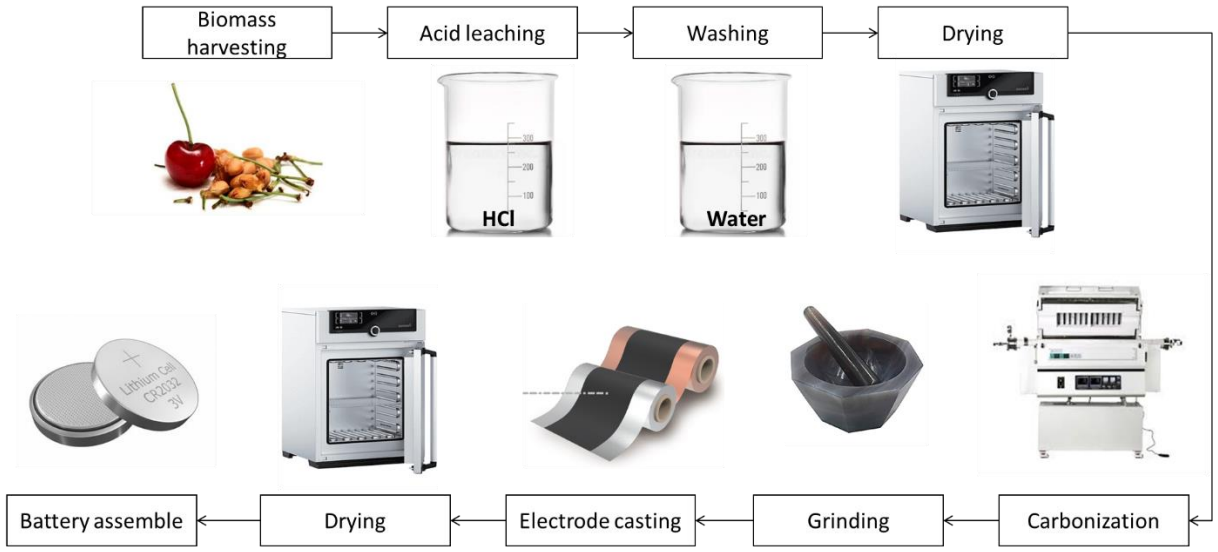

Figure 4. Hard carbon preparation and battery assembling roadmap.

3.1. Biowaste treatment

The main precursor of carbon source in this work is cherry pit. The first step of biomass processing is washing material with deionized water. Then in order to remove impurity, the material washed with 1M solution of hydrochloric solution. After leaching in acid, the material washed with deionized water until the pH value reached 7. In order to remove water content, the material dried in drying oven at 80 ^{o}C for 24 hours.

3.2. Doping procedure

The doping process is required to enrich the nitrogen content in hard carbon. The method of doping is solid state mixing of hard carbon precursor with dopant agent. As a dopant, urea was selected. The weight ratio between hard carbon precursor and dopant agent is 1:5. The high amount of dopant agent was selected in order to maximize the nitrogen content.

3.3. Synthesis of hard carbon

Carbonation of hard carbon is a thermal treatment process, where partial decomposition of material proceeds in a non-oxidative environment. As an environment, the argon gas was used with a purity of 99.987%. Synthesis of hard carbon proceeded in tubular furnace 1600 ^{o}C (1-Zone 80 mm OD Tube Furnace Across International with Eurotherm Controller). Material carbonized at

temperatures 800 ^{o}C, 1000 ^{o}C, 1200 ^{o}C, 1400 ^{o}C and 1500 ^{o}C, with heating rate 4 ^{o}C min^{-1} and dwelling time was 3 h.

3.4. Slurry preparation

In order to prepare the electrode, synthesized hard carbon was ground in agate mortar until the material becomes a powder. The process of slurry preparation proceeded in two mortars. In the first mortar hard carbon powder was mixed with acetylene black (AB) MTI Corporation to enhance conductivity. The second mortar is required to conduct a dissolution process of the binding agent in an organic solvent. The binder that was used is polyvinylidene fluoride (PVDF) Solef 5130, and the solvent was n-methyl-2-pyrrolidone (NMP) Sigma Aldrich. The role of PVDF is to improve the mechanical stability of electrodes by creating a polymeric matrix to trap hard carbon in it. After dissolving PVDF, a mixture of hard carbon and AB was added to the second mortar and stirred with a pestle until the suspension becomes homogeneous. The mass ratio of hard carbon, AB and PVDF is 80:10:10.

3.5. Electrode casting

The general structure of the electrode for rechargeable batteries is a foil of a current collector coated with a thin film of active material. The copper foil was used as the current collector. Prepared electrode slurry was placed on foil and with a micrometer adjustable film applicator (doctor blade) the smooth film was obtained. The thickness of the film was set to 25 microns on the doctor blade. After the application of the film, the electrode dried in a drying oven at 60 ^{o}C. During the drying process, NMP evaporates and the polymerization process of PVDF occurs.

3.6. Coin cell assembling

The geometry that was used for battery assembly is coin cell CR 2032. Figure 5 illustrates the components and structure of the coin cell. Coin cell cap, Belleville washer (spring) and spacer welded on welder UH-1001 Usutani at 2-4 voltage. The disk of the electrode was cut with a puncher and placed into a coin cell case. Further battery cell setup was done in a glove box under an argon atmosphere with a purity of 99.999%. The separator Absorbed Glass Mat was placed on top of the electrode disc, and 200 μL of electrolytes (sodium hexafluorophosphate) was added. On top of the separator the sodium thin disk as a counter electrode was placed. The sodium disk was prepared by mechanically rolling and cutting sodium metal. After placing the sodium disk, the cap was installed and sealed in the pressing machine.

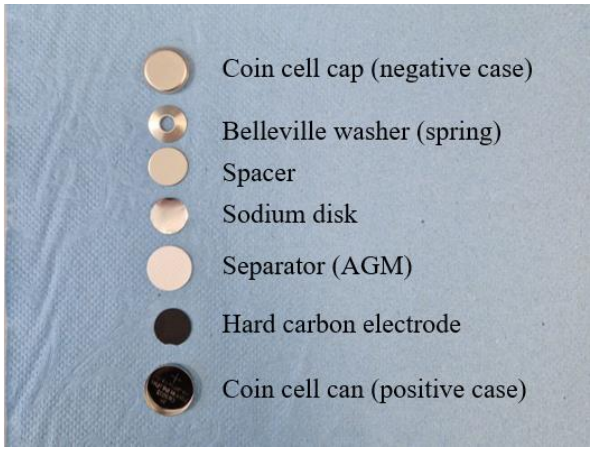

Figure 5. Coin cell structure and particles.

3.6. Material characterization.

X-ray diffraction (XRD) analysis was done on an X-ray Diffraction (XRD) System - SmartLab (Rigaku), in order to identify the interplanar spacing of material. The Raman spectroscopy LabRAM (Horiba) was used to study the graphitization degree of material, the used wavelength of the laser beam was 514.5 nm. The surface morphology of the material was examined by scanning electron microscope (SEM) ZEISS Crossbeam 540, and the internal structure was studied by transmission electron microscope (TEM) JEOL JEM - 1400 Plus. A galvanostatic charge-discharge test was conducted to identify the electrochemical performance of the electrode on the WonATech WBCS3000Ls32 battery test system.

Chapter 4 - Results and discussion

4.1. Morphology analysis by SEM and TEM.

The morphology of materials was examined via SEM and TEM analysis. Figure 6 represented the surface morphology of bare hard carbon that carbonized at 1000 ^{o}C, 1200 ^{o}C and 1400 ^{o}C. Material structure is not uniform and has irregular shapes. Based on Figure 6, the structure of derived hard carbon remains from the cherry pit. In macro scale material has pores and cavities with a diameter in a range of 5-20 micrometers, which is clearly seen in Figure 6 d,e. The cavities are filled with small hard carbon particles, the appearance of small particles is the result of material crushing during the grinding process. In the microscale, the material has pores with diameters from 1 to 0.4 micrometers. Based on heating temperature no significant effect was observed on macrostructure and microstructures.

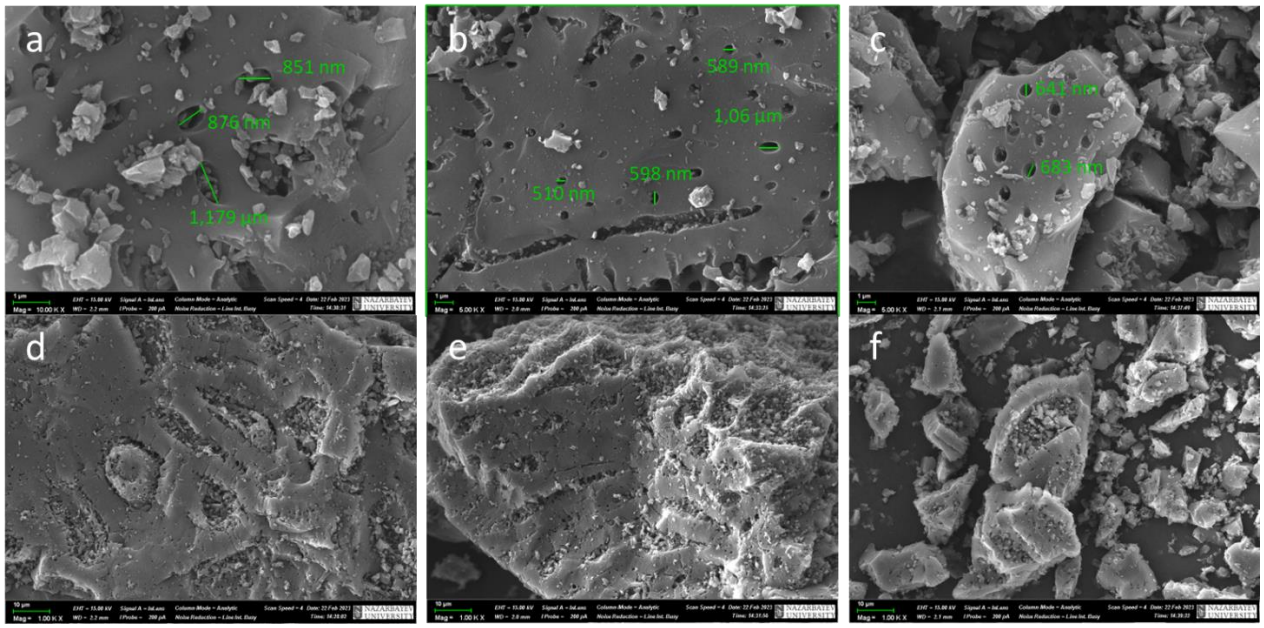

Figure 6. SEM image of cherry pit derived hard carbon without doping temperatures 1000^{o}C (a,d), 1200^{o}C (b,e) and 1400^{o}C (c,f).

The structural morphology of the material was examined by transmission electron microscope (TEM). In Figure 7 TEM image of bare hard carbon carbonized at 1000 ^{o}C, 1200 ^{o}C and 1400 ^{o}C is illustrated. Based on the results, at 1000 ^{o}C there observed the amorphous structure and disordered pattern of carbon sheets (Figure 6 a,b), and no pseudo graphitic structure was observed. At a temperature of 1200 ^{o}C there observed that carbon sheets aligned and stacked together by creating a pseudo graphitic structure (Figure 6 c,d). At 1400 ^{o}C the length of aligned carbon sheets is increased, and the amount of pseudo graphitic domains become higher.

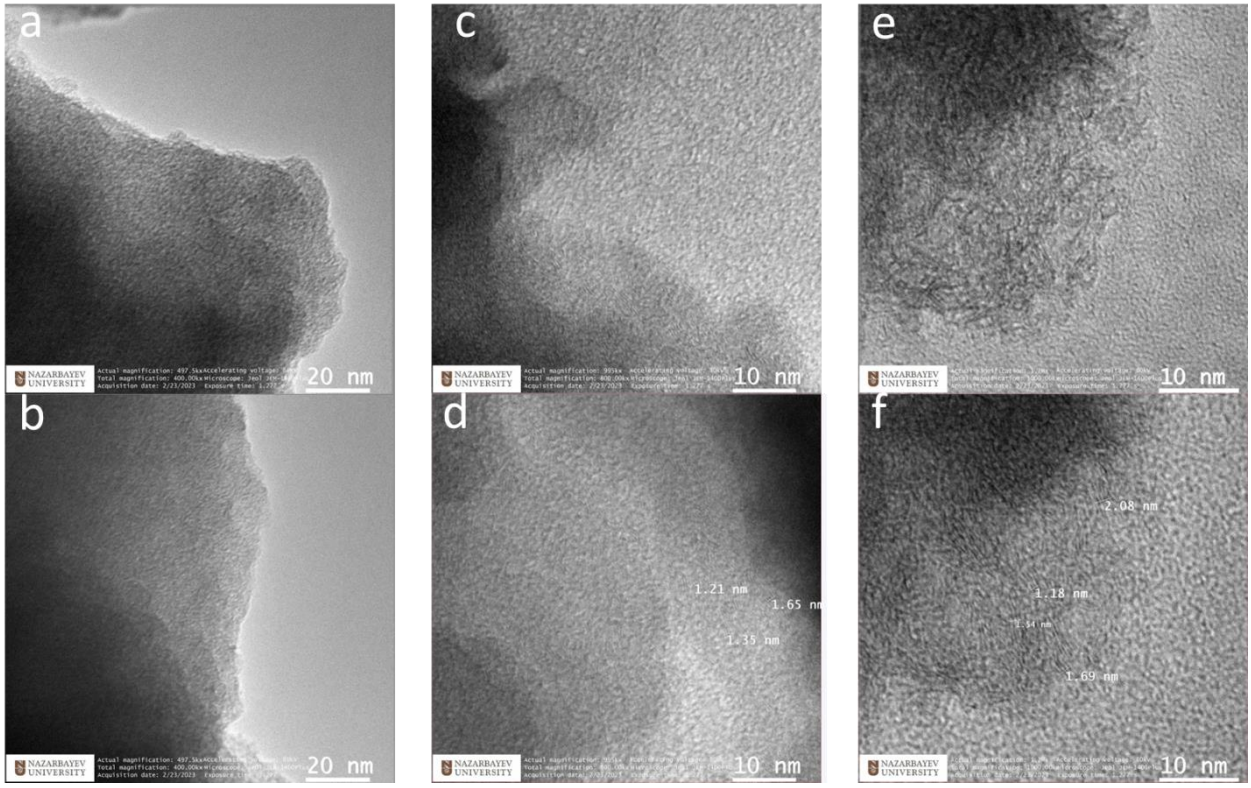

Figure 7. TEM image of bare cherry pit derived hard carbon temperatures 1000 ºC (a,b), 1200 ºC (c,d) and 1400 ºC (e,f).

4.2. XRD analysis of hard carbon.

XRD analysis was done for bare hard carbon at temperature range 800 ºC, 1000 ºC,1200 ºC, and 1400 ºC (Figure 8). XRD pattern of hard carbon has wide low peaks that indicate the amorphous structure of the material. The peak that appears at 22º corresponds to the (002) plane, and the peak at 44 º (100) plane. The slight shifting of XRD patterns to the right side was observed with temperature increment. It indicates that an increment in temperature decreases the interplanar spacing [37]. The detailed peak positions are represented in Table 2. Based on the XRD pattern the interplanar spacing between carbon sheets was identified by using the Braggs law.

$$n\lambda = 2 * d * \sin(\theta)$$

$$d = \frac{\lambda}{2\sin(\theta)}$$

Where lambda indicates X-ray wavelength 0.15418 nm, d corresponds to interplanar spacing. The interplanar spacing of bare hard carbon from 0,388 nm to 0.380 nm by increasing carbonation temperature from 800 ºC to 1400 ºC. However, some contradicting results were observed on a pattern

of doped materials. Nitrogen-doped materials interplanar spacing decreased. It could be a result of the induced graphitization of carbon content from the dopant agent. The XRD pattern of post-doping shows that no significant effect was observed on the spacing of the graphitic layer.

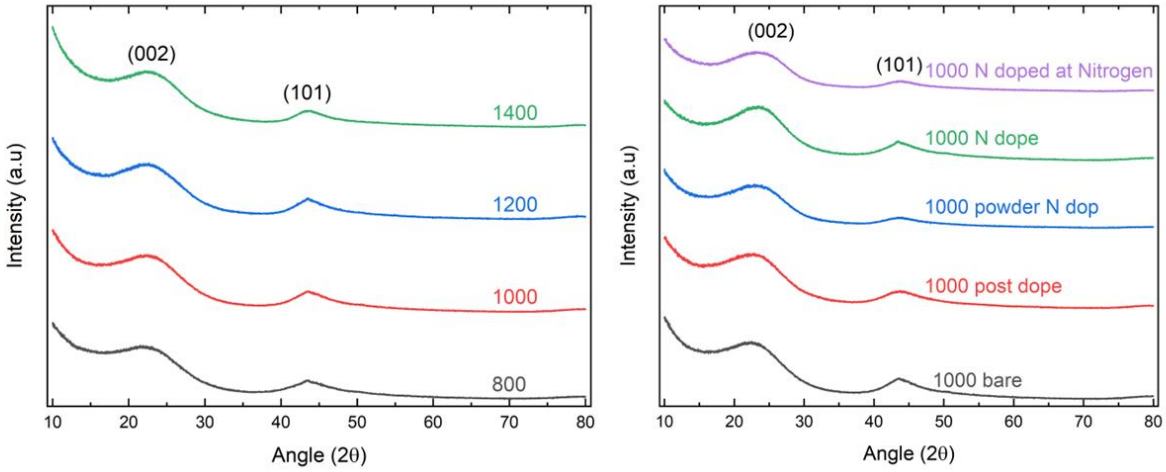

Figure 8. XRD pattern of cherry pit derived hard carbon, bare (a), doped at 1000 ºC(b) .

Table 2. Crystallite properties of hard carbon based on XRD.

Material name	L_c (nm)	L_d (nm)	Diffraction angle 2θ^o
800-bare	0,998786	0,388031	22,91835
1000-bare	0,940727	0,385284	23,08399
1200-bare	0,883708	0,384863	23,10958
1400-bare	0,932586	0,380308	23,39026
1000-postdope	0,972229	0,383414	23,19815
1000-powder-N-dope	1,001003	0,377431	23,57112
1000-N-dope	0,93187	0,371959	23,92296
1000-N-dope-N2	0,983853	0,372603	23,88098
1400-postdope	0,933883	0,373135	23,84647

4.3. Raman spectroscopy analysis of hard carbon.

Raman spectroscopy analysis was conducted in order to identify the graphitization degree of carbonaceous material (Figure 9). The Wavelength of the Raman laser beam was 515 nm. Raman spectrum shows two broad peaks that approximately shift at 1330 cm^{-1} and at 1580 cm^{-1} which corresponds to D and G bands. The D band represents the disordered structure of carbon sheets and the G band represents of the presence of pseudo-graphitic domains in the material. Figure 9 illustrated

Raman spectra of bare samples, with temperature increment there observed that the ratio of the areal intensity of G vs D bands increases, which indicates decrement of disorderness of structure and increment of graphitization degree [38]. In Figure 9 b, the results of the bare sample that carbonized at 1000 ^{o}C compared with different doping methods at the same temperature. Based on the ratio of the areal intensity of G vs D bands, doping of material affects graphitization degree, the area of the graphitic domain decreased in all N-doped material. The 1000-post-doped material shows the closest result to bare material, it is due to this material was carbonized first without nitrogen dopant and creating its structure and after carbonation it was undergone to post-doping. Based on Raman spectra the crystallite length in the lateral ab direction is identified according the following equation and represented in Table 3 [39].

$$L_a(nm) = (2.4 * 10^{-10}) * \lambda^4 * (\frac{I_G}{I_D})$$

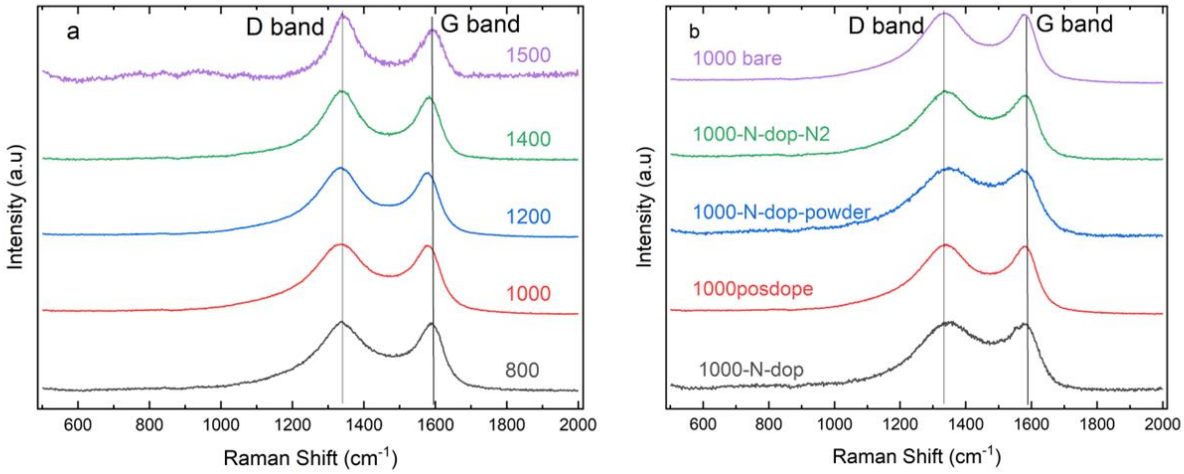

Figure 9. Raman spectra of bare hard carbon (a), and doped (b).

Based on table 3, the lateral length of crystallites increased with increment of carbonation temperature. Urea doping suppressed of carbon layer growth in lateral direction.

Table 3. Processed data from Raman spectra for La calculation.

material	Areal intensity D	Areal intensity G	I_G/I_D	L_a
800	25976,88	10386,74	0,399846	6,724268
1000	28070,11	10219,85	0,364083	6,122847
1200	23942,23	9557,2999	0,399182	6,713103

1400	20202,96	9572,817	0,473833	7,968519
1500	11592,45	6842,703	0,590272	9,926709
1000-N-dop	26486,9	8018,484	0,302734	5,091127
1000post-dope	24602,19	8215,403	0,33393	5,615751
1000-Ndop-powder	29354,07	7061,307	0,240556	4,045475
1000-N2	24450,94	7869,062	0,321831	5,412278

4.4. CHNS Elemental analysis of hard carbon.

Elemental analysis was done in order to identify the nitrogen content in hard carbon. The bare samples compared first to evaluate the nitrogen content in bare sample (Figure 10 a). There identified that sample carbonized at 800 ^{o}C has low nitrogen content, this could be caused by poor packing the powder into alumina foil. Based on remaining results of nitrogen, there observed that nitrogen content decreases with temperature increment, also sharp decrement observed between 1200 ^{o}C – 1400 ^{o}C and it could be a reason of significant differences in graphitization degree. The hydrogen content also decreases with temperature and reaches minimum value at 1400 ^{o}C. Decrement of heteroatoms form hard carbon causes the shrinking of interplanar spacing and morphology change. The doped hard carbon analyzed, all doped materials carbonized at 1000 ^{o}C shows high nitrogen content 4.1-5.7% (Figure 10 b). There were observed interesting trend among post doped materials, the nitrogen content of post doped material is lower, especially for 1400 ^{o}C. Based on this result there could be assumed that nitrogen dopant precursor reacts with hard carbon on the surface, in case of post doping, the surface of hard carbon already shrinks and less reactive for doping.

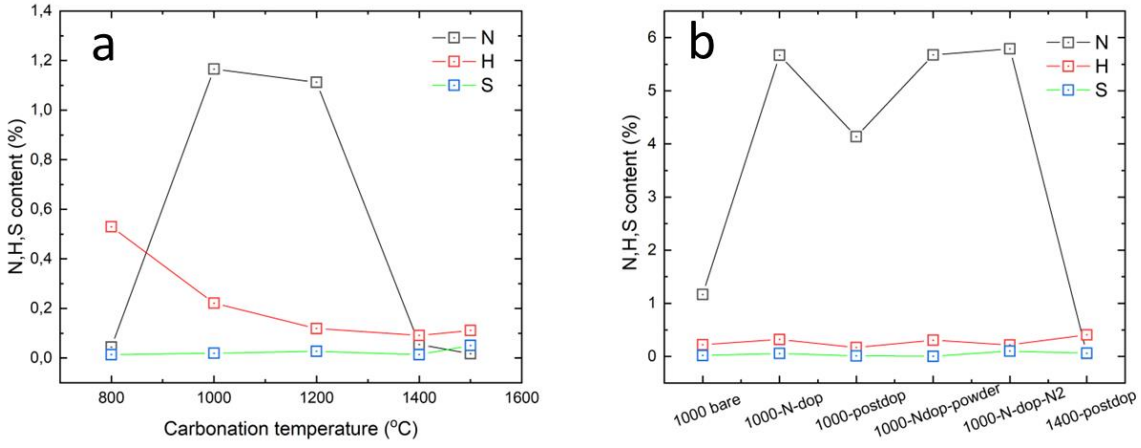

Figure 10.Elemental composition of hard carbon, a- bare, b-nitrogen doped.

4.5. Galvanostatic charge-discharge test.

The charge-discharge test was performed for identifying the energy capacity of the prepared electrodes. First, the effect of carbonization temperature was tested. Figure 11 illustrates the first 2 cycles of bare hard carbon charge-discharge profiles. The test was performed at a low current density of 20 mA g^{-1}, it was selected to eliminate mass transfer limitation and identify the full capacity of the material. From TEM analysis no defined graphitic domain was observed and it is correlated with the electrochemical performance of hard carbon 1000 ^{o}C and 800 ^{o}C, lack of graphitic domain results in small or absence of slope capacity. With an increment of carbonization temperature, there observed an increment of capacity, mainly the slope capacity. It correlates with the result of Raman spectra where with temperature the graphitization degree and lateral length of the graphitic domain are increased, and the higher lateral length of the graphitic domain provides a higher intercalation surface for sodium ions. Also, the initial columbic efficiency is increasing, due to the decrement of surface area at high temperatures.

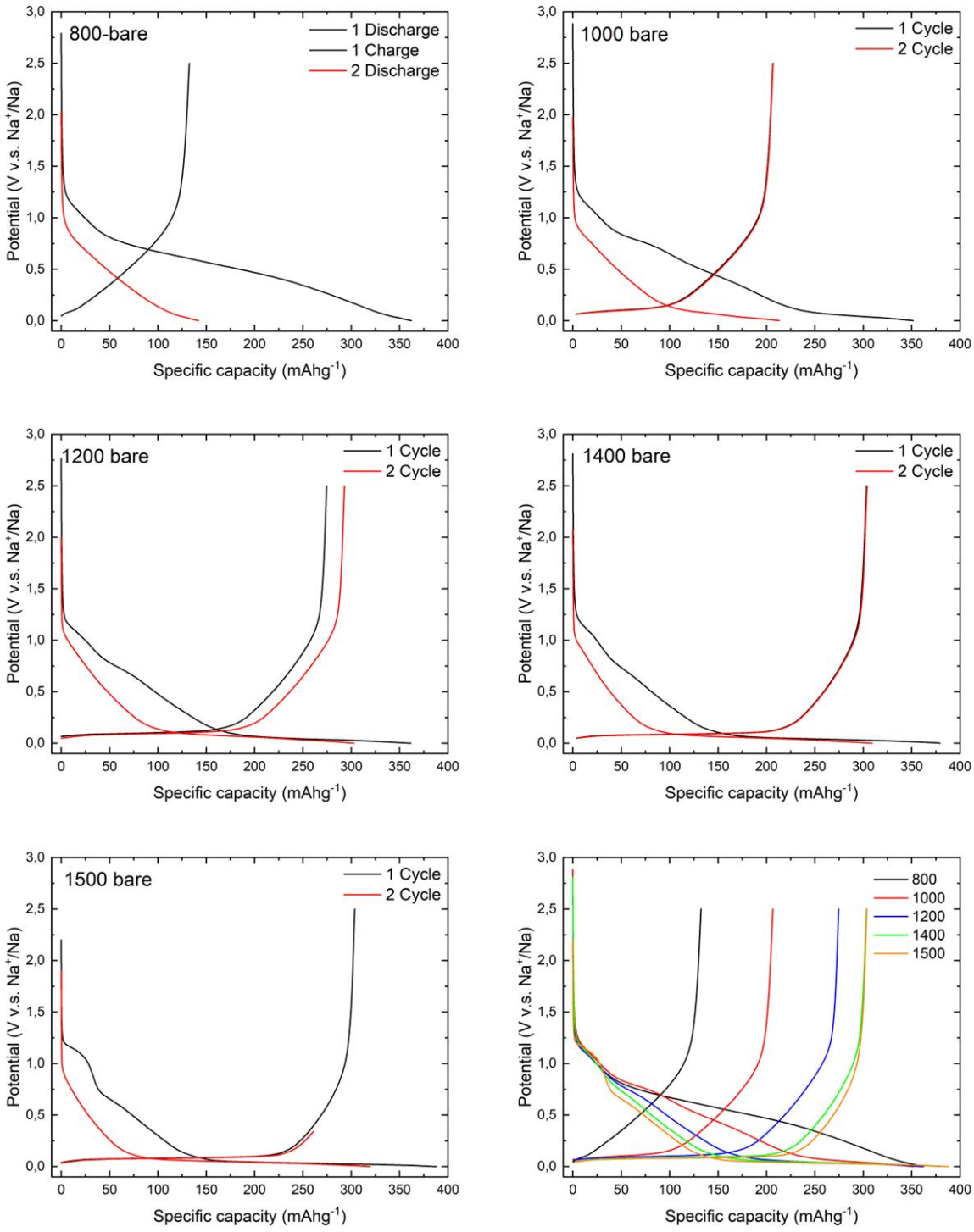

Figure 11. Galvanostatic charge-discharge test of bare hard carbon at different temperature.

The 1000 ^{o}C carbonization temperature was selected for nitrogen doping, the selection criteria were based on the knowledge that higher temperature treatment decreases of heteroatom content of the material, and the objective was to obtain higher nitrogen content in the material. Three different

nitrogen doping method was examined, first was dry mixing urea with cherry pit and carbonization at argon atmosphere, second was mixing with urea and carbonization at nitrogen and the third was post doping (Figure 12). The material doped in a nitrogen atmosphere exhibited poor capacity, based on the charge-discharge test there observed that the selection of atmosphere affected on material morphology. Nitrogen doping with urea under an argon atmosphere slightly improves the slope capacity of the material, which indicates that the surface of the material was modified and improved the adsorption and desorption processes. Also, a slight improvement of ICE indicates a surface effect. The post-doping of the material shows further improvement in the electrochemical performance of hard carbon. The high capacity of post-doping is the result of moderate graphitization, high interplanar spacing, and surface doping with nitrogen.

Table 4. Summary on electrochemical performance of cherry pit derived hard carbon.

Material	Irreversible capacity (mAh g^{-1})	Reversible capacity (mAh g^{-1})	ICE (%)	Plateau capacity 0V -0.1V (mAh g^{-1})	Slope capacity 0.1V-2.5V (mAh g^{-1})
800	362,29	132,48	36,57	36,58	95,90
1000	351,59	206,64	58,77	111,18	95,47
1200	361,65	274,57	75,92	186,02	88,54
1400	382,22	304,84	79,75	215,42	89,42
1500	388,04	318,67	78,26	265,11	52,56
1000-N-N2	401,46	67,57	16,83	41,82	25,75
1000-N-dop	344,98	219,77	63,71	127,63	92,14
1000-postdope	379,24	263,60	69,51	143,13	120,47

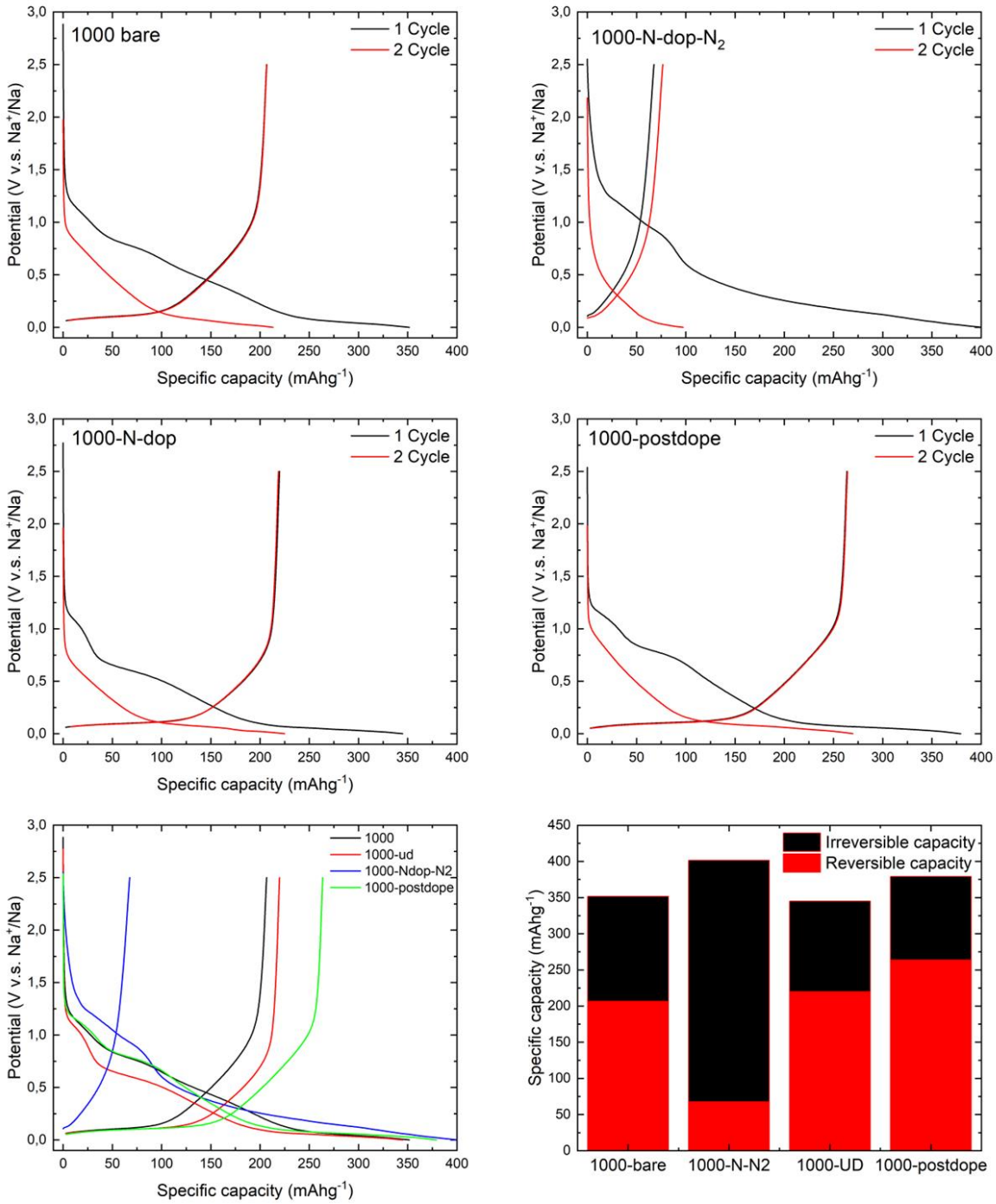

Figure 12. Electrochemical performance of doped hard carbon at 1000 ºC.

4.6. Cyclic stability at different charge rate.

The hard carbon material prepared at temperatures 1400 °C and 1500 °C showed highest results in low current rate, however it only provides information about maximum capacity of electrode. In order to obtain complete electrochemical performance of materials batteries tested at 5 different current rate 20 mA g^{-1}, 50 mA g^{-1}, 100 mA g^{-1}, 500 mA g^{-1} and 1000 mA g^{-1} (Figure 13). The hard carbon derived at 1500 °C has the highest capacity 305 mAh g^{-1} at 50 mA g^{-1} current rate, at 100 mA g^{-1} the capacity decreased to 244 mAh g^{-1}. This decrement is result of concentration polarization on the surface of electrodes. The transition moment from 100 mA g^{-1} to 500 mA g^{-1} shows significant drop in capacity of hard carbons derived 1400 °C and 1500 °C. Unfortunately, batteries with hard carbon 1200 °C shorted. The huge capacity decrement at 500mA g^{-1} is probably result of mass transfer limitation, due to insufficient time for adsorption of sodium into inner part of hard carbon and for intercalation reaction. It means that at high current rate adsorption proceeds only on easy assessable surface of hard carbon. At 1 A g^{-1} capacity drop to 53 mAh g^{-1}. All bare electrodes show similar behavior and capacity at 1 A g^{-1}, however nitrogen post doped hard carbon shows good capacity retention 110 mAh g^{-1} at 1 A g^{-1}. Probably the reason of such improvement of electrochemical performance at high current rate is nitrogen doping enhanced surface of material.

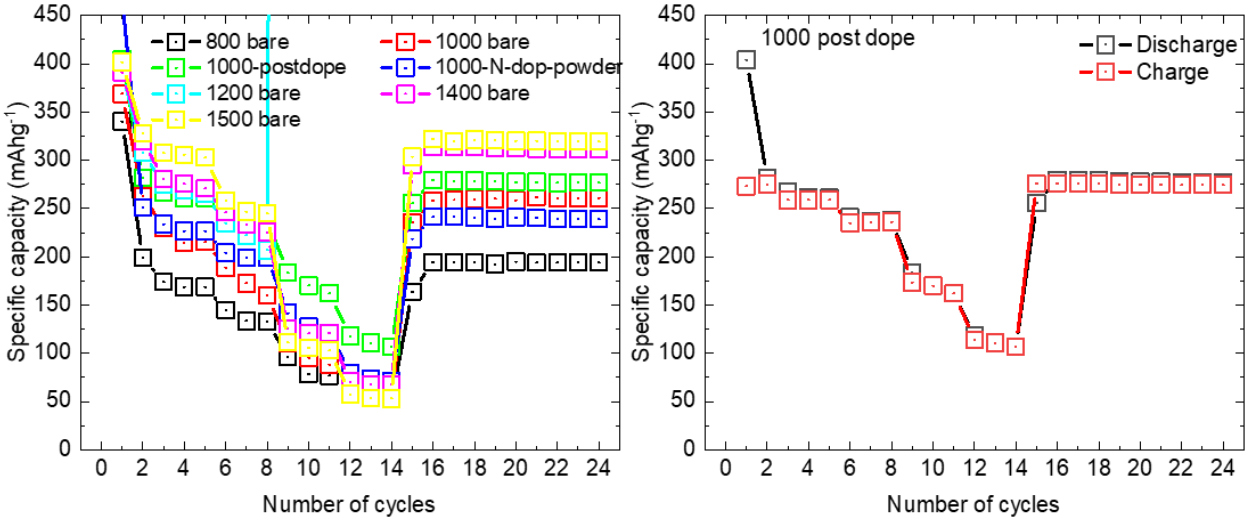

Figure 13. Electrochemical performance of cherry pit derived hard carbon at different current rate.

4.7. Comparison of result with other work.

The cyclic stability test provided information of electrochemical performance of hard carbon derived in this work. In order evaluate performance it is required to compare with results of other work (Table 5).

Mangosteen derived hard carbon provided capacity 180 and 330 at temperatures 1000 ^{o}C and 1500 ^{o}C. In this work at 1000 ^{o}C with nitrogen doping 263 mAh g^{-1} obtained, and bare material at 1500 ^{o}C provided 319 mAh g^{-1}. From wood Shen et.al. obtained 260 mAh g^{-1} capacity, the method that was used is oxidation by adding oxidation reagent. Pomelo peel derived hard carbon shows impressive capacity, activation with phosphoric acid strategy was used to obtain such performance. Cotton derived hard carbon at 1300 ^{o}C by Li et.al. illustrates good capacity at current rate 30 mA g^{-1}, however at lower temperatures the significant decrement of specific capacity was observed. Best electrochemical performance of cellulose derived hard carbon observed at carbonization temperature range of 1400-1600 ^{o}C.

Table 5. Electrochemical performance comparison with other work

Material	Temperature ^{o}C	Reversible capacity mAh g^{-1}	Current rate mA g^{-1}	ICE (%)	Reference
Mangosteen	1000	180	20	55	[40]
Mangosteen	1500	330	20	83	[40]
Wood	1000	260	20	72	[41]
Pomelo peels	700	236	200	27	[42]
Hollow carbon nanofiber	700	174	50	41	[43]
N-doped porous hollow carbon nanofibers	700	190	50	32	[43]
Cotton	1300	315	30	83	[44]
Cotton	1000	88	30	26	[44]
Cellulose	1600	310	37	83	[45]
Cherry pit N doped	1000	259	50	69	This work
Cherry pit bare	1500	318	20	79	This work

Chapter 5 – Conclusion

In summary, the hard carbon material was successfully synthesized by simple pyrolysis method for SIB, and temperature effect was analyzed. The various nitrogen doping method was used to improve electrochemical performance of hard carbon. SEM, TEM, XRD, Raman spectroscopy, CHNS analysis was done for material characterization.

- Based on study identified that doping with nitrogen suppress graphitic crystallites growth in hard carbon, which decreases possible intercalation slots for sodium ions. However, availability of those graphitic crystallite for sodium intercalation is also important parameter
- Based on galvanostatic charge-discharge analysis there identified that carbonization at 1500^{o}C provides the highest capacity, at higher temperature the size of graphitic domain was increased and plateau capacity increased, however the slope capacity decreased by limiting adsorption-desorption process.
- According charge-discharge analysis best doping method was nitrogen post doping of hard carbon after its synthesis. The post doped hard carbon at 1000 ^{o}C improves material capacity from 206 mAh g^{-1} to 236 mAh g^{-1}. The nitrogen doping slightly improved ICE of sample 1000^{o}C, however to obtain better ICE high temperature treatment is required, which decreases heteroatom content in material. Further study is required to identify the galvanostatic charge-discharge performance of synthesized material at high current rate.
- Cycling of battery at different current rate provided information that, post doping with nitrogen improves capacity at high current rate. Based on all analysis there observed that post doping with nitrogen improves the surface of hard carbon by improving adsorption of sodium ions.

References

[1] R. Lee, "The outlook for population growth," *Science*, vol. 333, no. 6042. pp. 569–573, Jul. 29, 2011. doi: 10.1126/science.1208859.

[2] M. Balat, "Electricity from worldwide energy sources," *Energy Sources, Part B: Economics, Planning and Policy*, vol. 1, no. 4, pp. 395–412, Dec. 2006, doi: 10.1080/15567240500400879.

[3] S. N. Seo, "Beyond the Paris Agreement: Climate change policy negotiations and future directions," *Regional Science Policy and Practice*, vol. 9, no. 2, pp. 121–140, Jun. 2017, doi: 10.1111/rsp3.12090.

[4] Y. Nishi, "The development of lithium ion secondary batteries," *Chemical Records*, vol. 1, no. 5, pp. 406–413, 2001, doi: 10.1002/tcr.1024.

[5] J. B. Goodenough, "Rechargeable batteries: Challenges old and new," *Journal of Solid State Electrochemistry*, vol. 16, no. 6, pp. 2019–2029, Jun. 2012, doi: 10.1007/s10008-012-1751-2.

[6] J. Asenbauer, T. Eisenmann, M. Kuenzel, A. Kazzazi, Z. Chen, and D. Bresser, "The success story of graphite as a lithium-ion anode material-fundamentals, remaining challenges, and recent developments including silicon (oxide) composites," *Sustainable Energy and Fuels*, vol. 4, no. 11. Royal Society of Chemistry, pp. 5387–5416, Nov. 01, 2020. doi: 10.1039/d0se00175a.

[7] J.-M. Tarascon and M. Armand, "WSPC-MATERIALS FOR SUSTAINABLE ENERGY-Reprint Volume Book-Trim Size:-11in x 8.5in Issues and challenges facing rechargeable lithium batteries," 2001. [Online]. Available: www.nature.com

[8] T. Kim, W. Song, D. Y. Son, L. K. Ono, and Y. Qi, "Lithium-ion batteries: outlook on present, future, and hybridized technologies," *Journal of Materials Chemistry A*, vol. 7, no. 7. Royal Society of Chemistry, pp. 2942–2964, 2019. doi: 10.1039/C8TA10513H.

[9] H. Ambrose and A. Kendall, "Understanding the future of lithium: Part 1, resource model," *J Ind Ecol*, vol. 24, no. 1, pp. 80–89, Feb. 2020, doi: 10.1111/jiec.12949.

[10] S. O. Altiparmak, "China and Lithium Geopolitics in a Changing Global Market," *Chinese Political Science Review*, 2022, doi: 10.1007/s41111-022-00227-3.

[11] G. Martin, L. Rentsch, M. Höck, and M. Bertau, "Lithium market research – global supply, future demand and price development," *Energy Storage Mater*, vol. 6, pp. 171–179, Jan. 2017, doi: 10.1016/j.ensm.2016.11.004.

[12] X. Zhang, A. Han, and Y. Yang, "Review on the production of high-purity lithium metal," *Journal of Materials Chemistry A*, vol. 8, no. 43. Royal Society of Chemistry, pp. 22455–22466, Nov. 21, 2020. doi: 10.1039/d0ta07611b.

[13] J. F. Peters, A. P. Cruz, and M. Weil, "Exploring the economic potential of sodium-ion batteries," *Batteries*, vol. 5, no. 1, Mar. 2019, doi: 10.3390/batteries5010010.

[14] A. R. Nurohmah *et al.*, "Sodium-ion battery from sea salt: a review," *Materials for Renewable and Sustainable Energy*, vol. 11, no. 1. Springer Science and Business Media Deutschland GmbH, pp. 71–89, Apr. 01, 2022. doi: 10.1007/s40243-022-00208-1.

[15] N. Yabuuchi, K. Kubota, M. Dahbi, and S. Komaba, "Research development on sodium-ion batteries," *Chemical Reviews*, vol. 114, no. 23. American Chemical Society, pp. 11636–11682, Dec. 10, 2014. doi: 10.1021/cr500192f.

[16] H. Zhang, I. Hasa, and S. Passerini, "Beyond Insertion for Na-Ion Batteries: Nanostructured Alloying and Conversion Anode Materials," *Advanced Energy Materials*, vol. 8, no. 17. Wiley-VCH Verlag, Jun. 15, 2018. doi: 10.1002/aenm.201702582.

[17] F. Klein, B. Jache, A. Bhide, and P. Adelhelm, “Conversion reactions for sodium-ion batteries,” *Physical Chemistry Chemical Physics*, vol. 15, no. 38, pp. 15876–15887, Oct. 2013, doi: 10.1039/c3cp52125g.
[18] Y. Xu, Y. Zhu, Y. Liu, and C. Wang, “Electrochemical performance of porous carbon/tin composite anodes for sodium-ion and lithium-ion batteries,” *Adv Energy Mater*, vol. 3, no. 1, pp. 128–133, Jan. 2013, doi: 10.1002/aenm.201200346.
[19] A. Rudola, K. Saravanan, C. W. Mason, and P. Balaya, “Na2Ti3O7: An intercalation based anode for sodium-ion battery applications,” *J Mater Chem A Mater*, vol. 1, no. 7, pp. 2653–2662, Feb. 2013, doi: 10.1039/c2ta01057g.
[20] W. Zhang, F. Zhang, F. Ming, and H. N. Alshareef, “Sodium-ion battery anodes: Status and future trends,” *EnergyChem*, vol. 1, no. 2, p. 100012, Sep. 2019, doi: 10.1016/j.enchem.2019.100012.
[21] W. Wang *et al.*, “Advances of TiO2 as Negative Electrode Materials for Sodium-Ion Batteries,” *Advanced Materials Technologies*, vol. 3, no. 9. Wiley-Blackwell, Sep. 01, 2018. doi: 10.1002/admt.201800004.
[22] M. Winter, J. O. Besenhard, M. E. Spahr, and P. Novák, “Insertion electrode materials for rechargeable lithium batteries,” *Advanced Materials*, vol. 10, no. 10, pp. 725–763, 1998, doi: 10.1002/(SICI)1521-4095(199807)10:10<725::AID-ADMA725>3.0.CO;2-Z.
[23] B. Jache and P. Adelhelm, “Use of graphite as a highly reversible electrode with superior cycle life for sodium-ion batteries by making use of co-intercalation phenomena,” *Angewandte Chemie - International Edition*, vol. 53, no. 38, pp. 10169–10173, Sep. 2014, doi: 10.1002/anie.201403734.
[24] H. Moriwake, A. Kuwabara, C. A. J. Fisher, and Y. Ikuhara, “Why is sodium-intercalated graphite unstable?,” *RSC Adv*, vol. 7, no. 58, pp. 36550–36554, 2017, doi: 10.1039/c7ra06777a.
[25] Y. Cao *et al.*, “Sodium ion insertion in hollow carbon nanowires for battery applications,” *Nano Lett*, vol. 12, no. 7, pp. 3783–3787, Jul. 2012, doi: 10.1021/nl3016957.
[26] D. A. Stevens and J. R. Dahn, “The Mechanisms of Lithium and Sodium Insertion in Carbon Materials,” *J Electrochem Soc*, vol. 148, no. 8, p. A803, 2001, doi: 10.1149/1.1379565.
[27] “FORMATION OF GRAPHITE STRUCTURE IN CARBON CRYSTALLITES 929.”
[28] D. A. Stevens and J. R. Dahn, “High Capacity Anode Materials for Rechargeable Sodium-Ion Batteries You may also like The Mechanisms of Lithium and Sodium Insertion in Carbon Materials,” 2000.
[29] X. Dou *et al.*, “Hard carbons for sodium-ion batteries: Structure, analysis, sustainability, and electrochemistry,” *Materials Today*, vol. 23. Elsevier B.V., pp. 87–104, Mar. 01, 2019. doi: 10.1016/j.mattod.2018.12.040.
[30] S. Komaba *et al.*, “Electrochemical Na insertion and solid electrolyte interphase for hard-carbon electrodes and application to Na-ion batteries,” *Adv Funct Mater*, vol. 21, no. 20, pp. 3859–3867, Oct. 2011, doi: 10.1002/adfm.201100854.
[31] C. Bommier, T. W. Surta, M. Dolgos, and X. Ji, “New Mechanistic Insights on Na-Ion Storage in Nongraphitizable Carbon,” *Nano Lett*, vol. 15, no. 9, pp. 5888–5892, Sep. 2015, doi: 10.1021/acs.nanolett.5b01969.
[32] X. Chen *et al.*, “Understanding of the sodium storage mechanism in hard carbon anodes,” *Carbon Energy*, vol. 4, no. 6. John Wiley and Sons Inc, pp. 1133–1150, Nov. 01, 2022. doi: 10.1002/cey2.196.
[33] Y. Li *et al.*, “Regulating Pore Structure of Hierarchical Porous Waste Cork-Derived Hard Carbon Anode for Enhanced Na Storage Performance,” *Adv Energy Mater*, vol. 9, no. 48, Dec. 2019, doi: 10.1002/aenm.201902852.

[34] N. Zhang *et al.*, “High capacity hard carbon derived from lotus stem as anode for sodium ion batteries,” *J Power Sources*, vol. 378, pp. 331–337, Feb. 2018, doi: 10.1016/j.jpowsour.2017.12.054.
[35] R. R. Gaddam *et al.*, “Spinifex nanocellulose derived hard carbon anodes for high-performance sodium-ion batteries,” *Sustain Energy Fuels*, vol. 1, no. 5, pp. 1090–1097, 2017, doi: 10.1039/c7se00169j.
[36] A. Agrawal, S. Janakiraman, K. Biswas, A. Venimadhav, S. K. Srivastava, and S. Ghosh, “Understanding the improved electrochemical performance of nitrogen-doped hard carbons as an anode for sodium ion battery,” *Electrochim Acta*, vol. 317, pp. 164–172, Sep. 2019, doi: 10.1016/j.electacta.2019.05.158.
[37] E. Irisarri *et al.*, “Optimization of Large Scale Produced Hard Carbon Performance in Na-Ion Batteries: Effect of Precursor, Temperature and Processing Conditions,” *J Electrochem Soc*, vol. 165, no. 16, pp. A4058–A4066, 2018, doi: 10.1149/2.1171816jes.
[38] J. Han, I. Johnson, Z. Lu, A. Kudo, and M. Chen, “Effect of Local Atomic Structure on Sodium Ion Storage in Hard Amorphous Carbon,” *Nano Lett*, vol. 21, no. 15, pp. 6504–6510, Aug. 2021, doi: 10.1021/acs.nanolett.1c01595.
[39] J. S. Weaving *et al.*, “Elucidating the sodiation mechanism in hard carbon by operando raman spectroscopy,” *ACS Appl Energy Mater*, vol. 3, no. 8, pp. 7474–7484, Aug. 2020, doi: 10.1021/acsaem.0c00867.
[40] K. Wang *et al.*, “Low-Cost and High-Performance Hard Carbon Anode Materials for Sodium-Ion Batteries,” *ACS Omega*, vol. 2, no. 4, pp. 1687–1695, Apr. 2017, doi: 10.1021/acsomega.7b00259.
[41] F. Shen *et al.*, “Chemically Crushed Wood Cellulose Fiber towards High-Performance Sodium-Ion Batteries,” *ACS Appl Mater Interfaces*, vol. 7, no. 41, pp. 23291–23296, Oct. 2015, doi: 10.1021/acsami.5b07583.
[42] K. L. Hong *et al.*, “Biomass derived hard carbon used as a high performance anode material for sodium ion batteries,” *J Mater Chem A Mater*, vol. 2, no. 32, pp. 12733–12738, Aug. 2014, doi: 10.1039/c4ta02068e.
[43] L. Zeng, W. Li, J. Cheng, J. Wang, X. Liu, and Y. Yu, “N-doped porous hollow carbon nanofibers fabricated using electrospun polymer templates and their sodium storage properties,” *RSC Adv*, vol. 4, no. 33, pp. 16920–16927, 2014, doi: 10.1039/c4ra01200c.
[44] Y. Li, Y. S. Hu, M. M. Titirici, L. Chen, and X. Huang, “Hard Carbon Microtubes Made from Renewable Cotton as High-Performance Anode Material for Sodium-Ion Batteries,” *Adv Energy Mater*, vol. 6, no. 18, Sep. 2016, doi: 10.1002/aenm.201600659.
[45] V. Simone, A. Boulineau, A. de Geyer, D. Rouchon, L. Simonin, and S. Martinet, “Hard carbon derived from cellulose as anode for sodium ion batteries: Dependence of electrochemical properties on structure,” *Journal of Energy Chemistry*, vol. 25, no. 5, pp. 761–768, Sep. 2016, doi: 10.1016/j.jechem.2016.04.016.

Appendices

Appendix A

Here represented full data of cyclic stability test at different scan rate of hard carbon materials.

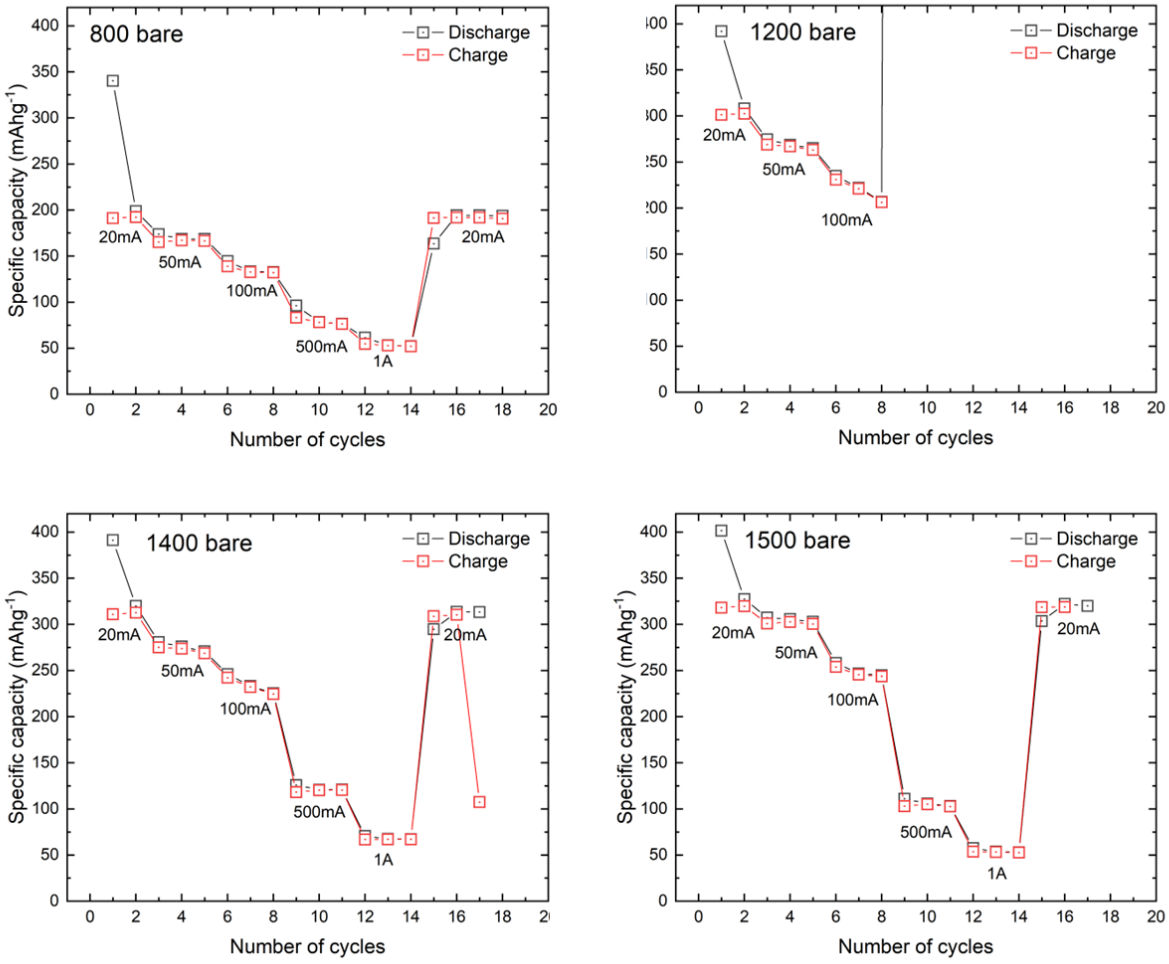

Figure A. 1. Battery cyclic performance at different scan rates.

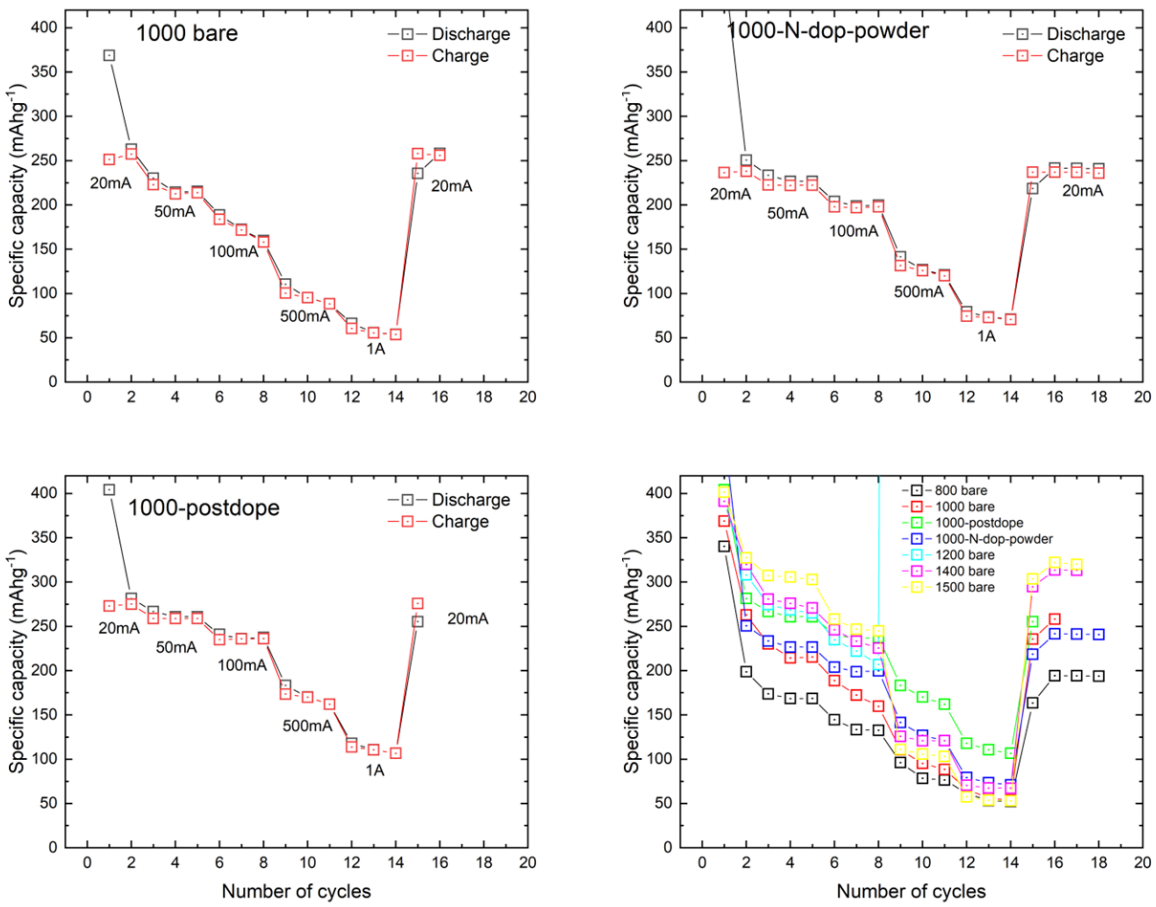

Figure A. 2.Cyclic performance at different scan rate electrodes derived at 1000 ºC.